EVIDENCE ON SIZES AND FRAGMENTATION OF THE NUCLEI OF COMET SHOEMAKER-LEVY 9 FROM HUBBLE SPACE TELESCOPE IMAGES

ZDENEK SEKANINA

Jet Propulsion Laboratory
California Institute of Technology
Pasadena, California 91109

Expanded version of a presentation at
the European Shoemaker- Levy 9/Jupiter Workshop
European Southern Observatory's Headquarters
Garching bei München, Germany
13-15 February 1995

Submitted to
Astronomy & Astrophysics
(Main Journal)

January 1995

Abstract

Central regions on the digital maps of 13 nuclear condensations of Comet Shoemaker–Levy 9. obtained with the Planetary Camera of the Hubble Space Telescope on' January 24-25, March 28--36, and July 4,1994, have been analyzed with the aim to identify the presence of distinct, major fragments in each condensation, to deconvolve their contributions to the signal that also includes the contribution from a surrounding cloud of dust (modeled as an extended source, using two different laws), to estimate the dimensions of the fragments and to study their temporal variations, and to determine the spatial distributions of the fragments as projected onto the plane of the sky. The deconvolution method applied is described and the results of the analysis are summarized, including the finding that sizable fragments did survive until the time of atmospheric entry. This result does not contradict evidence of the comet's continuing, apparently spontaneous fragmentation, which still went on long after the extremely close approach to Jupiter in July 1992 and which, because of the jovian tidal effects, may even have intensified in the final days before the crash on Jupiter. On plausible assumptions, the largest fragments are found to have had effective diameters of ~4 km as late as March and even early July)994. In most condensations, several sizable companions (~1 km or more across) have been detected within ~1000 km of the projected location of the brightest fragment and the surrounding dust cloud has been found to be centered on a point that is shifted in the general direction of the tail, probably due to effects of solar radiation pressure. Since the developed approach is based on certain premises and involves approximations, the results should be viewed as preliminary and the problem should be a subject of further investigation.

1. INTRODUCTION

The nuclear size is one of the fundamental bulk properties of every comet, Its knowledge is essential not only for our understanding of the object's observed physical behavior, but is also critical for theories of comet formation and long-term evolution. In the case of Comet Shoemaker–Levy 9 (1993e), a further incentive for pursuing all avenues available to addressing this problem was provided by the need to interpret the observed events that accompanied the comet's collision with Jupiter in July 1994. The masses of the major fragments, closely related to their dimensions, are the only inadequately known quantities preventing us from deriving reliable estimates for the kinetic energies of the individual nuclei and for the total energy deposited by them in the jovian atmosphere.

A number of estimates for the nucleus dimensions of the parent comet and/or its fragments can be found in the literature (Scotti & Melosh 1993; Weaver et *al.* 1994; Asphaug & Benz 1994; Chernetenko & Medvedev 1994; Solem 1994; Sekanina et *al.* 1994). The results fall into two distinct groups, the ranges for the effective diameter being, respectively, 1–2 km and 7–10 km for the parent comet and correspondingly smaller for its major fragments.

2. THE PROBLEM

The sizes of some of the comet's fragments are derived in this study photometrically from images obtained between January 27 and July 4, 1994 with the Planetary mode Charge Coupled Device (CCD) of the Wide-Field Planetary Camera 2 (WFPC-2) of the Hubble Space Telescope (HST), whose pixel size equals 0.0455 arcsec. The basic *modus operandi* can be compared with that of Weaver *et* al. (1994) and the reader is referred to this paper for information on the image calibration and processing. However, the analytical approach, applied here to extract the contributions from major fragments hidden in the surrounding cloud of dust, is very different from Weaver et *al.*'s technique, as will become apparent below. In addition, of course, the installation of the WFPC-2 in December 1993 resulted in a dramatic improvement of the HST's imaging quality in 1994.

The observed surface-brightness distribution in each condensation can in general be considered to consist of a convolved sum of contributions from a number of point sources (major fragments) and a number of extended sources (which make up the surrounding cloud of minor fragments and other particulate material). Available in practice were digital maps of brightness distributions in fields of 15 pixels, or 0.7 arcsec, across and centered on the peak pixel. In the absence of major deviations from an isotropic decrease in brightness from the peak pixel toward the field's edges on the majority of these digital maps, it was believed that the most appropriate samples to be employed in the analysis were made up of pixels encompassed in an area that was approximately circumscribed by a circle 15 pixels in diameter and centered on the peak. Samples satisfying this condition turned out to consist of 157 pixels, arranged successively in 15 rows (or columns) of 3, 7, 9, 11, 13, 13, 15, 15, 15, 13, 13, 11, 9, 7, and 3. Except in a few particular cases (notably for the condensation S), such samples were used throughout this investigation.

It should be mentioned at the outset that in practice all models that involved more than one extended source failed to result in successful solutions because of intractable convergence difficulties. The following description is thus limited to models with a multitude of point sources and a single extended source. The approach has two important

features: (a) it allows the location of the extended source's brightness peak to differ from the location of any of the point sources and (b) it also allows pixel interpolation, taking into account the fact that the location of any source (including the peak of the extented source) does not generally coincide with the center of a pixel. Instead, the coordinates of the source locations are solved for by least squares along with the other parameters (Sees. 3-5). In practical applications, these two features were found to be indispensable for a successful solution optimization,

3. THE POINT SOURCES

Let $B(X, Y)$ be the observed amount of light impinging on a square-shaped pixel in a row X and a column Y, measured in CCD analog-to-digital intensity units (ADU). The problem is to find summary contributions from the individual point sources and the extended source to the observed brightness distribution by integrating them over all pixels in the field and to determine the dimensions (effective diameter) of each point source from its integrated signal and an assumed albedo.

Consider first point sources. The need to solve for the location of each source and to maintain the problem easily tractable dictated that a simple empirical function be found that would reasonably well fit a model point spread function's (PSF) pixel-signal distribution that was available in tabular form. After extensively experimenting with a wide variety of candidate functions, I settled on the following quasi-Gaussian approximation for the PSF'S surface-brig}~tness distribution law $b_{\rm psf}(x, y)$, expressed in ADU per arcsec^2:

$$b_{\rm psf}(x,y) = b_* \exp\left[-\left(\frac{x^2+y^2}{2\sigma_{\rm psf}^2}\right)^{\nu_{\rm psf}}\right], \tag{1}$$

where $\sigma_{\rm psf} > 0$ is the PSF's dispersion parameter (in arcsec), $\nu_{\rm psf} > 0$ is a dimensionless constant ($\nu_{\rm psf} = 1$ for the Gaussian function), and $(x^2+y^2)^{1/2} = \rho$ is the angular distance (in arcsec) from the PSF's peak. The surface brightness at the peak is $b_{\rm psf}(0, O) = b_*$. The total signal, or the integrated brightness, I_* of a point source is, in ADU,

$$I_* = 2\pi \int_0^\infty \rho\, b_{\rm psf}(\rho)\, d\rho = 2\pi b_* \sigma_{\rm psf}^2\, \nu_{\rm psf}^{-1}\, \Gamma(\nu_{\rm psf}^{-1}), \tag{2}$$

where I'(z) is the Gamma function of argument z:

$$\Gamma(z) = \int_0^\infty t^{z-1} e^{-t} dt \qquad (z > 0). \tag{3}$$

If {X*, Y_* } are the pixel location numbers of a given source (or its PSF's peak signal), the $\{x, y\}$ coordinates of the center of an {X, Y} pixel relative to this source are:

$$\begin{aligned} x &= \Pi(X - X_*) \\ y &= \Pi(Y - Y_*), \end{aligned} \tag{4}$$

where 11 is the pixel size in arcsec. The pixel locations {X, Y} have been defined by assigning the coordinates {10, 10} to the center of the peak pixel.

Applied to the available PSF pixel distribution for a point source whose I_* = 500 ADU (close to the maximum integrated brightness encountered among the studied fragments), the introduced approximate solution yielded, with 11 = 0.0455 arcsec, the following best-fit parametric values: σ_{psf} = 0.0112 ± 0.0009 arcsec, ν_{psf} = 0.34'7 ± 0.011, and therefore I_* = 0.004085 b^*. The PSF'S contribution of 93.4 ADU to the brightest pixel represents 18.7 percent of the entire signal and implies a peak surface brightness of 253 ADU/pixel^2 or, equivalently, 122,000 ADU/arcsec2 The pixel coordinates of the PSF's peak came out to be X_* = 9.992 ± 0.011 and Y_* = 10.025 ± 0.011, so the source's introduced position was recovered with a formal precision of 0.03 pixel or 0.001 arcsec. This error is considerably smaller than the actual uncertainties involved. The solution leaves a mean pixel-signal, residual of ±0.86 ADU and a maximum residual of 3 ADU, as seen from the map of the residuals presented in Table 1. The maximum residual is slightly lower than the expected peak noise assuming no contribution from fiat-fielding and about $\frac{1}{2}$ the expected peak noise if the flat-fielding noise is 5 percent of the signal. Measured by these standards, the employed quasi-Gaussian law should be considered as more than adequate for the purposes of this study. Nevertheless, the law's approximate character is reflected in an uncertainty of about ±1O ADU, or 2 percent of the total signal I_*, in the case under consideration. The relative uncertainty of the derived signal should be higher for fainter sources and for sources located in high-density areas of the dust cloud, primarily because of higher levels of noise. A more elaborate approximation law is discussed in Sec. 7.

TABLE 1

Pixel Distribution of the Brightness Residuals (in ADU) From the PSF's Best-Fit Quasi-Gaussian Law Approximation for a Point Source Whose I^* = 500 ADU.

X (pixels)	Y (pixels) 3 4 5 6 7 8 9 10 11 12 13 14 15 16 17	X (pixels)
3	0 0 0	3
4	0 0 0 0 0 0 0	4
5	0 0 0 0 0 0 0 0 0	5
6	0 0 0 – 1 - 1 - 1 - 1 0 0 0 0	6
7	0 0 0 – 1 – 1 – 1 - 1 - 1 – 1 – 1 0 0 0	7
8	0 0 0 –1 +1 +1 0 +2 +1 0 0 0 0	8
9	0 0 0 - 1 –1 +2 –3 +1 -343 0 0 0 0 0	9
10	0 0 o–l–1 o +2 0 “0+2 o 0 0 0 0	10
11	0 0 0 - 1 – 1 o – 3 0 –3 +3 0 0 0 0 0	11
12	0 O – l – 1 0 +2 +2 +3 +1 0 0 0 0	12
13	0 0 o–1 -1 0 0 o–1 o 0 0 0	13
14	0 0 0 0 0 0 – 1 0 0 0 o	14
15	0 0 0 0 0 0 0 0 0	15
16	0 0 0 0 0 0 0	16
17	0 0 0	17

4. THE EXTENDED SOURCE

Two different laws have been considered for the surface-brightness distribution $b_{ext}(\rho)$ of the extended source. Convoluted with the PSF, the laws are assumed in the form:

$$\text{Law A}: b_{ext}(\rho) = \frac{b_0}{1+(\rho/\sigma)^{\nu}}, \qquad \text{Law B}: \quad b_{ext}(\rho) = b_0 \exp\left[-\left(\frac{\rho^2}{2\sigma^2}\right)\right], \qquad (5)$$

where p is the angular distance from the point of peak surface brightness, $b_{ext}(0) = b_0$, of the extended source, located at a pixel position $\{X_o, Y_o\}$. The dispersion σ and the exponent ν (analogous, in the case of the law B, to σ_{psf} and ν_{psf}), as well as b_0, X_0, and Y_0 are constants to be determined by a least-squares differential- correct ion procedure. The integrated brightness of the extended source is:

$$\text{Law A}: I_0 = 2\pi^2 b_0 \sigma^2 \nu^{-1} \operatorname{cosec}(2\pi/\nu) \text{ for } \nu > 2, \quad I_0 \to \infty \text{ for } \nu \leq 2. \qquad \text{Law B}: I_0 = 2\pi b_0 \sigma_2 \iota^{-1} \Gamma(\nu^{-1}), \qquad (6)$$

As in the case of a point source, the $\{x, y\}$ coordinates of the center of an {X, Y} pixel relative to the peak of the extended source are

$$x = \text{II}(X - X_0)$$
$$y = \text{II}(Y - Y_0). \qquad (7)$$

5. THE SOLUTION

The observed pixel-signal distribution can now be modeled as a sum of the contributions from n point sources and the extended source. If the pixel location of an ith point source is given by $\{(X_*)_i, (Y_*)_i\}$ and its surface-brightness distribution by $b^{(i)}_{psf}(x, y)$, the modeled distribution is calculated by the following integration over each pixel's area:

$$B(X, Y) = \sum_{i=1}^{n} \left\{ \int_{\text{II}[X-(X_*)_i-\frac{1}{2}]}^{\text{II}[X-(X_*)_i+\frac{1}{2}]} \int_{\text{II}[Y-(Y_*)_i-\frac{1}{2}]}^{\text{II}[Y-(Y_*)_i+\frac{1}{2}]} b^{(i)}_{psf}(x, y)\, dy + \int_{\text{II}(X-X_0-\frac{1}{2})}^{\text{II}(X-X_0+\frac{1}{2})} dx \int_{\text{II}(Y-Y_0-\frac{1}{2})}^{\text{II}(Y-Y_0+\frac{1}{2})} b_{ext}(x, y)\, dy, \right. \qquad (8)$$

where the location of the peak of the extended source is allowed to differ from the location of any of the considered point sources, X'. # $(X_*)_i$ and Y. $\neq (Y_*)_i$, $(i = 1, \ldots, n)$.

A solution for $B(X, Y)$ that includes n point sources and an extended source has $(3n+5)$ parameters: $(I_*)_1, \ldots, (I_*)_n, (X_*)_1, \ldots, (X_*)_n$, (Y..)l, $\ldots$ $(Y_*)_n, b_0, \sigma, \nu, X_0$, and Y_0. let the observed distribution $B(X, Y)$ be approximated by a $\mathcal{B}(X, Y)$ array of the summed up contributions from the n point sources and the extended source, calculated with an initial set of values of the (3n + 5) parameters. An improved set of values of these parameters, $(I_*)_i + (\Delta I_*)_i, (X_*)_i + (\Delta X_*)_i, (Y_*)_i + (\Delta Y_*)_i (i = 1, \ldots, n), b_0 + \Delta b_0$, $\sigma + \Delta\sigma, \nu + \Delta\nu, X_0 + \Delta X_0$, and $Y_0 + \Delta Y_0$, results from the equations of condition for the individual parametric corrections. These equations are applied to all pixels that contain information deemed useful for deconvolving the contributions from the various sources. For an {X, Y} pixel the equation of condition is:

$$13(x, Y) - \mathcal{B}(X, Y) = \sum_{i=1}^{n} \left[\left(\frac{\partial \mathcal{B}}{\partial I_*} \right)_i (\Delta I_*)_i + \left(\frac{\partial \mathcal{B}}{\partial X_*} \right)_i (\Delta X_*)_i + \left(\frac{\partial \mathcal{B}}{\partial Y_*} \right)_i (\Delta Y_*)_i \right] + \frac{\partial \mathcal{B}}{\partial b_0} \Delta b_0 + \frac{\partial \mathcal{B}}{\partial \sigma} \Delta \sigma + \frac{\partial \mathcal{B}}{\partial \nu} \Delta \nu + \frac{\partial \mathcal{B}}{\partial X_0} \Delta X_0 + \frac{\partial \mathcal{B}}{\partial Y_0} \Delta Y_0. \quad (9)$$

With the partial derivatives calculated numerically, the application of a least-squares differential-correction procedure allows one to iterate the solution until it has converged. If noise in the input data impedes the convergence, a more cautious approach should be applied by solving for only some of the parameters at any one time and to expand the number of parameters to $(3n + 5)$ gradually and only after the convergence is reached when solving for fewer than the full number of parameters. This approach is particularly appropriate in the early stages of the iteration procedure, before the solution has "settled" around the optimum parametric values, or when the convergence has been slow.

The experience with the calculations whose results are described in the next section suggests that the following general approach should be employed in analyzing the signal distribution from the data charts of the observed images:

Step 1 begins with a conservative assumption that the observed signal is due entirely to the extended source. one may have to start with solving for only some of the source's parameters but eventually does so for all five of them to find an initial solution and the distribution of pixel-brightness residuals.

Step 2 starts with an inspection of the pixel distribution of residuals from the available solution. This distribution is compared with the expected. instrumental noise variations. At very low signals, the noise is about 1 ADU, increasing to at least 2 ADU for a signal of 25 ADU, 3 ADU for 60 ADU, and 4 ADU for 110 ADU. On only a few occasions did the peak pixel's signal exceed this limit. If some residuals are significantly greater than the expected noise, especially if the distribution displays clumps of elevated (positive) values, an improved solution is desirable and the analysis continues. On the other hand, if the distribution indicates a satisfactory fit to the data set, the analysis is terminated. Continuing the analysis (cf. Step 3) in a case like this would invariably entail progressively growing convergence difficulties, which would force the procedure's termination anyway.

Step 3, initiated when the fit by the solution from Step 2 is deemed unsatisfactory, involves the introduction of a new point source to improve the distribution of pixel-signal residuals. The location of this source is first approximated by the coordinates of the pixel of maximum positive residual exhibited by the available distribution. Since the total brightness of this source is at this stage unknown, its initial value is merely a guess; zero is one of options that can be employed.

Step 4 is the search for an improved solution. It includes (a) the determination of the parameters for an expanded set of sources using the iterative least-squares differential-correction procedure and (b) the calculation of a new distribution of pixel-signal residuals. At this point one proceeds to Step 2 and the procedure is repeated from there on.

One could design other statistically diagnostic criteria for testing the significance of each solution. The ultimate goals of the error analysis effort arc to discriminate as fully as possible between genuine unresolved sources and artifacts of the applied procedure and to estimate the uncertainties involved in the results.

6. THE RESULTS

The described approach has been applied to digital maps of the brightness distribution on the images of several nuclear condensations of Comet Shoemaker–Levy 9, as observed with the HST Planetary Camera. Tables 2-7 and Figs. 1-3 present the results of these calculations. The effective diameters of the fragments are determined from their R magnitudes (derived from the ADU units and the exposure time with the use of a transformation formula), assuming a geometric albedo of 0.04 and a phase coefficient of 0.035 mag/deg. On these assumptions, the formal 1σ error in the calculated diameters is typically ± 0.1 to ± 0.2 km, but, realistically, diameters $\lesssim 1$ km can be at best only marginally detected.

For each of the nuclear condensations F, G, H, N, P_1, P_2, Q_1, Q_2, R, S, T, U, and V, observed with the HST on January 27, 1994, Table 2 compares the laws A and B [cf. Eq. (5)], assumed for the brightness distribution in the extended source, in terms of (a) an effective diameter calculated for the largest fragment and (b) a number of detected companions. It is noted that no point source is needed to fit satisfactorily the brightness distribution of the condensation V when the law A is applied; this is shown by assigning a value of <<1 km to the effective diameter of the largest fragment. When the law B is used, the detection is at best marginal, only at a 2σ level for the integrated brightness. The comparisons of columns 2 and 3 and also of columns 4 and 5 lead to an obvious conclusion that the results are for all practical purposes independent of the adopted law. However, it is obvious from the table that the mean residual from the law A is slightly better on the average, and never worse, than the mean residual from the law B, so the law A was adopted in subsequent calculations, whose results are in Tables 3 and 4.

Table 3 lists the effective diameter of the largest fragment and the number of companions detected in the HST digital maps of the comet's images taken on January 27,

TABLE 2

Comparison of Effective Diameters of Largest Fragments and Numbers of Companions Derived From HST Observations Made on J an. 27, 1994 Using Two Different Laws for Surface Brightness Distribution in Extended Source.

Condensation	Largest object's effective diameter (km)		Number of detected companions		Mean residual (ADU)	
	Law A	Law B	Law A	Law B	Law A	Law B
F	2.3	2.3	1	1	±0.96	±0.97
G	4.3	4.4	4	4	±1.26	±1.28
H	3.3	3.2	3	2	±1.19	±1.25
N	1.6	1.6	0	0	±0.79	±0.79
P_1	1.3	1.3	2	2	±0.96	±0.98
P_2	2.4	2.4	5	3	±0.88	±0.97
Q_1	4.0	4.0	5	5	±1.16	±1.17
Q2	3.2	3.2	2	2	3.0.91	±0.94
R'	2.7	2.8	0	0	±0.97	±1.02
R*	2.7	2.5	0	0	±1.19	±1.23
s	3.6	3.6	8	6	±1.09	±1.18
T	1.4	1.4	1	1	±0.80	±0.81
u	1.3	1.3	0	0	±0.69	±0.69
v	<<1	$\lesssim 1$	0	0	±0.83	±0.83

[a] From image on Q frame.
[b] From inage on S frame.

TABLE 3

Effective Diameters of Largest Fragments and Numbers of Companions From HST Observations (Extended Source Subtracted Using Law A).

Condensation	Largest object's effective diameter (km)			Number of detected companions		
	Jan. 27	Mar. 30	Jul. 4	Jan. 27	Mar. 30	Jul. 4
F	2.3	2.1	...	1	1	...
G	4.3	3.7	...	4	3	...
H	3.3	...	...	3	...	...
N	1.6	1.4	...	0	0	...
P_1	1.3	0.6	...	2	0	...
P_2	2.4	1.4	...	5	4	...
Q_1	4.0	2.9	3.9	5	2	5
Q_2	3.2	1.5	2.5	2	3	3
R	2.7	2.1	...	0	2	...
S	3.6	2.5	...	8	6[a]	...
T	1.4	...	...	1	...	...
U	1.3	1.0	...	0	0	...
V	$\ll 1$	...	...	0	...	...

[a] Effective diameter of the largest companion is 2.3 km.

March 30, and July 4, 1994. The data in columns 2-4 suggest that there is no systematic variation in the dimensions with time, Even though it appears that the calculated sizes of most of the fragments were smaller in March than in January, the data for the fragments Q_1 and Q_2, observed on all three dates, show that by July their January dimensions were at least partially "recovered" and that perhaps the variations could primarily be a rotational effect of strongly irregular shape. Likewise, the numbers of detected companions, in columns 5–7, do not exhibit any significant trend. It can be shown that at typical relative velocities of ~ 0.1 m/s the various companions detected at different times are in most cases likely to be unrelated; exceptions are discussed briefly in Sec. 7. The large numbers of companions present evidence for a continuing disintegration of the largest fragments in numerous discrete events. The dots in Table 3 indicate that no appropriate data are available.

Table 4 summarizes the apparent R magnitudes of all detected fragments and their calculated effective diameters. Dots indicate the unavailability of the relevant data for this study, while hyphens show the absence of additional fragments in the available data. A tendency is noticed for the presence of one dominant fragment in each condensation. Exceptions that involve relatively large fragments (>2 km across) are offered by the condensation P_2 on January 27 and by S on March 30, in both of which the two largest fragments are of similar size. It will be of interest to correlate any possible multiple impact events of the individual condensations with evidence from Table. 4.

A set of the solutions and the quality of their fit to the observed pixel-brightness distribution as the number of the assumed point sources increases is exemplified in Table 5. The listed solutions refer to the nucleus condensation H observed on January 27, 1994, are optimized over a set of 157 pixels centered on the brightest one, and the extended source's brightness distribution is approximated by the law A.

TABLE 4

Apparent Magnitudes and Effective Diameters of Fragments Derived From HST Observations (Extended Source Subtracted Using Law A).

Condensation	Fragment	Apparent R magnitude			Effective diameter (km)		
		Jan. 27	Mar. 30	Jul. 4	Jan. 27	Mar. 30	Jul. 4
F	1	24.65	24.23	...	2.3	2.1	...
	2	26.09	25.47	...	1.2	1.2	...
	3	–	25.50	...	–	1.2	...
G	1	23.28	23.08	...	4.3	3.7	...
	2	25.23	24.94	...	1.8	1.6	...
	3	25.79	25.00	...	1.4	1.5	...
	4	25.87	25.48	...	1.3	1.2	...
	5	26.39	–	...	1.0	–	...
H	1	23.89	,..	...	3.3	...	...
	2	25.29	...	...	1.7	...	...
	3	26.34	...	...	1.1	...	...
	4	26.64	...	...	0.9	...	...
N	1	25.37	25.10	...	1.6	1.4	...
P_1	1	25.89	26.96	...	1.3	0.6	...
	2	26.30	–	...	1.1	–	...
	3	26.48	–	...	1.0	–	...
P_2	1	24.54	25.13	...	2.4	1.4	. .
	2	24.88	25.89	...	2.1	1.0	...
	3	25.65	26.28	...	1.4	0.8	...
	4	25.99	26.38	...	1.2	0.8	...
	5	26.25	26.92	...	1.1	0.6	...
	6	26.44	–	...	1.0	–	...
Q_1	1	23.42	23.57	23.27	4.0	2.9	3.9
	2	24.80	25.43	24.96	2.1	1.2	1.8
	3	25.51	26.22	25.26	1.5	0.9	1.6
	4	25.70	–	25.52	1.4	–	1.4
	5	25.72	–	25.69	1.4	–	1.3
	6	26.22	–	26.56	1.1	–	0.9
Q2	1	23.95	24.97	24.25	3.2	1.5	2.5
	2	25.32	26.16	24.98	1.7	0.9	1.8
	3	25.62	26.46	25.47	1.5	0.8	1.4
	4	–	26.50	25.81	–	0.6	1.2
R	1	24.26	24.25	...	2.7	2.1	...
	2	–	25.75	...	–	1.1	...
	3		26.04	...	–	0.9	...
s	1	23.69	23.92	...	3.6	2.5	...
	2	25.54	24.06	...	1.5	2.3	...
	3	25.83	25.62	...	1.3	1.1	...
	4	25.98	25.72	...	1.2	1.1	...
	5	26.04	26.13	...	1.2	0.9	...
	6	26.14	26.15	...	1.2	0.9	...
	7	26.15	26.17	...	1.1	0.9	...
	8	26.18	–	...	1.1	–	...
	9	26.56	–	...	1.0	–	...
'l'	1	25.72	...	...	1.4	.	...
	2	27.16	...	...	0.7	...	...
u	1	25.92	25.80	...	1.3	1.0	...

TABLE 5

Set of Solutions for the Nuclear Condensation H, Observed by the HST's Planetary Camera on January 27, 1994, As a Function of the Number of Assumed Fragments (Law A).

Number of point sources assumed	Mean residual (ADU)	Point source				Extended source				
		Id.	I_* (10^3 ADU)	X_* (pixels)	Y_* (pixels)	b_0 (10^5 ADU/arcsec^2)	σ (arcsec)	ν	X_0 (pixels)	Y_0 (pixels)
0	±1.99	. . . . .		...	...	0.462 ± 0.022	0.056+ 0.005	1.22+ 0.04	10.22A 0.03	10.18+ 0.03
1	±1.44	a	0.233 ± 0.014	10.12 ± 0.05	9.62 ± 0.03	0.240 ± 0.012	0.119+ 0.009	1.38& 0.06	10.35+ 0.04	10.67+ 0.05
2	±1.27	a	0.259+ 0.012	10.25+ 0.03	9.60 ± 0.02	0.216 ± 0.010	0.127+ 0.010	1.30+ 0.06	10.51+ 0.05	10.81+ 0.06
		b	0.068+ 0.010	8.78 ● 0.12	10.43* 0.07					
3	±1.23	a	0.265+ 0.011	10.26+ 0.03	9.60 ± 0.02	0.212 ± 0.009	0.130 ± 0.009	1.31 ± 0.06	10.51 ± 0.05	10.86 ± 0.06
		b	0.070+ 0.009	8.77 ± 0.11	10.41+ 0.07					
		c	0.019 ± 0.006	11.32 ± 0.29	5.16 ± 0.40					
4	±1.19	a	0.272 ± 0.012	10.30 ± 0.03	9.62 ± 0.03	0.208 ± 0.009	0.128+ 0.009	1.26+ 0.06	10.57& 0.06	10.97+ 0.07
		b	0.075 ± 0.009	8.77 ± 0.10	10.48+ 0.07					
		c	0.021+ 0.006	11.34 ± 0.25	5.28 ± 0.28					
		d	0.028+ 0.00S	8.92 ± 0.35	8.68 ± 0.21					

The match is seen to improve dramatically after the first point source (identified by the letter a and equal to the major fragment 3.3 km in diameter; cf. Tables 2–4) has been introduced in the solution, indicating that the point source's existence cannot be ignored. Test runs have shown that if the extended source's brightness variation satisfied a law $p^{-\nu}$ (ν = const.) all the way to the central pixel, the value of the dispersion would have to be comparable with, or smaller than, the pixel size, that is, $\sigma \lesssim 0.046$ arcsec, in obvious contradiction to the optimum value listed in Table 5. Further improvements in the fit are apparent as contributions from additional point sources, identified by the letters b–cl, have been allowed for. As expected, the calculated contribution from the extended source gradually decreases as the number of introduced point sources increases. This drop is considerable after the first point source, but tapers off as more point sources are included. No converging solution could be found that would involve more than four point sources. The calculated integrated brightness of each point source appears to increase with the number of the assumed sources, but the rate of increase also tapers off as their number increases. The calculated positions of the point sources are seen to be, within the errors, rather consistent and essentially independent of the solution. The letter identification of the fragments has been introduced to emphasize the order in which they have been included in the solution, in contrast to their numerical identification used in Table 4 and organized in the order of decreasing size. For the condensation H, the correspondence between the two classifications is obviously: 1 = a, 2 = b, 3 = d, and 4 = c.

The gradual improvement in the quality of the fit to the observed signal distribution of the condensation H is apparent from Tables 6 and 7, which list four maps of the brightness residuals in the 157 pixels. Table 6 presents the maps for the solutions with no and one point source assumed, while Table 7 for two and four point sources assumed. The position of the brightest pixel is always given by X = Y = 10 pixels and the residuals are in the ADU units. Highlighted in each map is the most conspicuous clump of positive residuals, suggesting the presence of yet another point source. It is noted that the prominence of the clumps diminishes from an area of four neighboring pixels with a peak residual of +9 ADU and a minimum residual of +2 ADU in the map for the solution in which only the extended source was assumed, to an area of only two neighboring pixels with a peak residual of +3 ADU and the minimum residual of +2 ADU. Also noted in the map for the solution with no assumed point source is a strong systematic trend, from generally negative residuals in the region X <10 pixels, Y <10 pixels to generally positive residuals in the region X >10 pixels, Y >10 pixels. This asymmetry appears to be brought about by a slight displacement of the extended source, relative to the brightest point source, by approximately +0.3 pixel in the X coordinate and by a little more than +1 pixel in the Y coordinate. This direction is close to the projected antisolar direction and the detected displacement is likely to be a cumulative effect of solar radiation pressure on the particulate in the dust cloud, whose model the extended source represents.

Figure 1 depicts the best model for the brightness distribution near the center of the condensation H, observed with the Planetary Camera on January 27, 1994. The model includes the contributions from four point sources (the fragments a, b, c, and d) and an extended source (the surrounding dust cloud). With the model's parameters listed in Table 5, the contributions to the total signal of the brightest pixel are calculated to amount to $51\frac{1}{2}$ percent from the fragment a, $43\frac{1}{2}$ percent from the dust cloud, 4 percent from b, and 1 percent from d. It is noted that the peak-brightness area of the dust cloud appears in the figure only as a modest bulge on the slope of the PSF of the fragment a.

TABLE 6

Distribution of Pixel-Signal Residuals (in ADU) for the Nuclear Condensation H, Observed by the HST'S Planetary Camera on January 27, 1994, As a Function of the Number of Assumed Fragments.

Number of point sources assumed = *O* (Mean residual = ±1.99 ADU)																Number of point sources assumed = 1 (Mean residual = ±1.44 ADU)																
x (pixels)	Y (pixels)															x (pixels)	Y (pixels)																	
	3	4	5	6	7	8	9	10	11	12	13	14	15	16	17		3	4	5	6	7	8	9	10	11	12	13	14	15	16	17	
3							0	-1		0						3							o	–1		o							3
4							–1	–3	–4	–1	–1	o	+3			4							O	-	2	–	3	–	l	-	1	0	+	2	4
5							-2	–2	–3	–2	–2	-3	–1	0	-2	5							–1	-1	–2	–2	–2	–3	–1	–1	–2			5
6							O	–	2	–	2	–	4	-	3	O	0	–1	+1	+1	6							+1	–1	–2	–1	–3	–2	0	O	–	2	O	0	6
7						–1	o	–1	–3	–2	–3	–1	+1	–1	o	0	0+2	7						0	+1	0	–	2	-	1	–	2	0	+1	–1	–1	0	–1	+2	7
8						O	O	–	3	–	2	–	3	–	1	0	+ 2 + 1 + 2 + 1 + 1 + 3	8						o	+1	-1	–1	-1	+1	+1	+3	+1	+1	o	0	+	2	8
9				+1	-1	+2	-2	–1	–1	+2	+2	+1	O	+4	+1	+1	+1 +1	9			+1	O	+3	-1	+1	+1	+2	+4	+3	–1	+3	O	–1	O	0					9
10				+1	-1	0	–3	–2	–3	+9	+1	–6	-1	+1	+2	+4	+2 +2	10			+1	0	+1	–2	0	-	2	–	1	–	2	-	1	-	3	–	1	0	+	2	+	1	+	1	10
11				+1	o	+1	o	–4	–4	+4	–2	–3	+3	+2	+3	+4	+3 +3	11			+1	+1	+2	+2	-2	-3	+3	+2	–1	+1	o	+1	+2	+2	+2					11
12					–1	+1	o	–2	–1	–1	–2	+1	O	+2	+3	+3	+1	12				0	+2	+1	o	0	0	–1	+1	–2	0	+1	+1	o							12
13					+2	–1	–1	–1	–1	0	0	–1	+1	+1	0	+1	+2	13				+2	0	–1	0	0	0	0	–2	0	0	–2	0	+1							13
14						o	0	–1	o	o	–1	–1	+1	+2	–1	+1		14					+1	o	–	1	0	4	1	–	1	–	2	0	+1	–2	o					14
15						-1	0	+1	o	–1	+2	+1	o	+2				15					0	+	1	+	1	0	–1	+1	+1	–1	+1								15
16							o	+2	+1	+1	+3	+1	+2					16							+1	+2	+1	o	+3	+1	+1										16
17								+2	+1	+1								17							+2	+1	o													17

TABLE 7

Distribution of Pixel-Signal Residuals (in ADU) for the Nuclear Condensation H, Observed by the HST'S Planetary Camera on January 27, 1994, As a Function of the Number of Assumed Fragments.

Number of point sources assumed = 2 (Mean residual = +1.27 ADU)		Number of point sources assumed = 4 (.Mean residual = ±1.19 ADU)	
X (pixels)	Y (pixels) 3 4 5 6 7 8 9 1 0 1 1 1 2 1 3 1 4 1 5 1 6 1 7	Y (pixels) 3 4 5 6 7 8 9 1 0 1 1 1 2 1 3 1 4 1 5 1 6 1 7	X (pixels)
3	o-1 0	0-1 0	3
4	0 –2 –3 –1 –1 0 +2	O – 2 - 3 - l – 1 0 + 2	4
5	–1 –1 -2 –1 –1 –2 –1 **O** -2	-1 –1 -2 –1 -1 –2 –1 **O** -2	5
6	+1 –l–1 O–3–2 O 0-1 0 0	+ 1 0 –1 0 –2 –1 +1 +1 –1 o 0	6
7	0+1 o-2 o–2 0 +1 –1 o 0 –1 +1	0+1 o–2 o–1 0+2 o 0 0 –1 +1	7
8	O +1 –i 0 0 +1 –1 +1 +1 i-2 0 0 +2	+1 +1 –1 0 –1 +1 –1 +1 +1 +2 0 0 +2	8
9	+1 0 +3 0 +1 +2 +3 o 0 –1 +3 o–I o 0	+1 0+3 0 +1 o 0 o–1 0+3 o–1 0 –1	9
10	+1 0 +1 –1 +1 –1 –1 0 +1 –2 o 0 +2 0 +1	+1 o 0 –2 +1 –1 o 0 +1 –2 0 0 +2 0 + 1	10
11	+1 +1 +3 +2 –2 –2 +1 0 –1 +1 0 +1 +2 +1 +1	+1 0 0 0 –2 –2 +1 –1 –1 +1 0 +1 +2 +1 +1	11
12	0 +2 +1 0 0 +1 –1 +1 –2 0 +1 +1 –1	–1 o 0 0 +1 +1 0 +1 –2 0 +1 +1 –1	12
13	+2 0 0 0 0 +1 o–2 0–1-2–1 o	+2 -1 -1 0 +1 +1 +1 – 1 o – l – 2 – 1 o	13
14	0 O–i o +1 –1 –2 0 0 - 3 – 1	0 0 0 +1 +1 –1 –1 0 0 –3 –1	14
15	–1 o +1 0 –1 +1 o - 1 0	0 +1 +1 0 –1 +1 o – 1 o	15
16	0+2 o 0+2 0 +1	0+2 o 0+2 0 +1	16
17	+1 +1 o	+1 +1 0	17

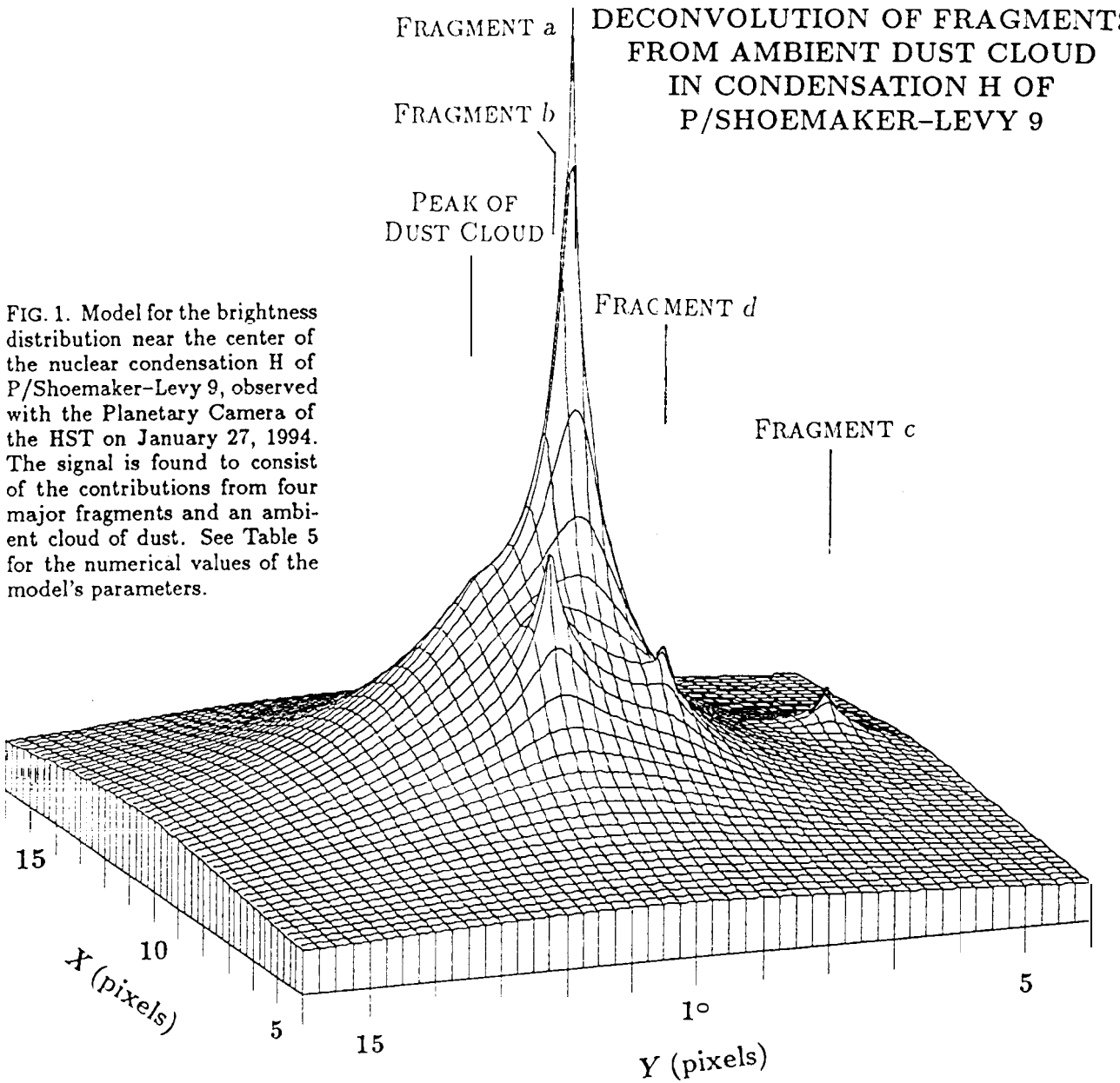

FIG. 1. Model for the brightness distribution near the center of the nuclear condensation H of P/Shoemaker–Levy 9, observed with the Planetary Camera of the HST on January 27, 1994. The signal is found to consist of the contributions from four major fragments and an ambient cloud of dust. See Table 5 for the numerical values of the model's parameters.

7. DISCUSSION AND CONCLUSIONS

The results of this investigation indicate that prolific fragmentation of the comet's nucleus continued for a considerable period of time after the initial tidal breakup in July 1992, so that the dimensions of the individual fragments were time dependent. The process of fragmentation, while essentially continuous taken stochastically, appears to have proceeded—at least in its early stages, involving large, kilometer-sized fragments-in the form of discrete events, which can readily explain the repeatedly observed instances of sudden, short-term brightening of the various condensations. There is little doubt that, as a result of the fragmentation events recurring over and over again, many of the objects eventually disintegrated to the extent that they could. no longer be detected individually even on a condensation's digital map and, sooner or later, they merely contributed to the surrounding dust cloud. However, available evidence shows that, in spite of the progressive fragmentation, one dominant fragment persisted in most condensations. Two striking exceptions to this rule are provided by the condensations P_2 and S. Weaver (1994a, b) remarked on a peculiar appearance of both of them: P_2 was clearly double on March 30, 1994, while a "spur" extending from S to the south was seen both on January 27 and March 30, but was brighter on the first date. The present analysis suggests that the two major components of P_2 were present already in late January, 0.135 arcsec apart, with the fainter one at a position angle of 235°. The spur of the fragment S appears on digital maps to have consisted of four approximately aligned components 0.08 to 0.31 arcsec away from the brightest fragment on January 27 and the two innermost companions may have been identical with some of the fragments detected two months later. By then, however, the primary nucleus of S was found to have broken into two about equally bright components, separated by 0.05 arcsec, or some 160 km in projection onto the sky plane, and each of a calculated effective diameter of $\sim$2.5 km. The slightly fainter one of the two was at a position angle of $\sim$140°. All these developments are depicted in Figs. 2 and 3, which show the projected spatial distribution of companions and the position of the dust cloud's brightness peak relative to the primary nucleus in each condensation on, respectively, January 27 and March 30, 1994. The projected distances involved are typically hundreds of kilometers and up to 1000–1500 km.

Although the dimensions of individual fragments must obviously have diminished with time, no systematic rate of decrease could be established from the available data between late January and early July 1994. In fact, shortly before their crash on Jupiter, the largest fragments were still found to have effective diameters comparable with those derived by Weaver *et al.* (1994) from the HST observations in July 1993 and consistent with the dimensions of the comet's parent nucleus proposed by Sekanina et al. (1 994). The rate of decrease in the sizes of the large fragments, implied by their continuing breakups, appears to be much less significant than rotation variations in the projected cross-sectional area of these objects which undoubtedly were extremely irregular.

The dust clouds in most of the condensations are seen in Figs. 2 and 3 to be centered on points that arc located generally to the west of the brightest fragments, which was the direction of the tails and which is consistent with the presence of a slight cumulative effect duc to solar radiation pressure from the time of tidal breakup in July 1992. This effect's predicted direction is 273° on January 27 and 269° on March 30, 1994, and its presence is not surprising, if assemblages of particulate material in the condensations were dominated by ccntimctcr-sized pebbles.

RELATIVE POSITIONS OF FRAGMENTS AND EXTENDED-SOURCE PEAKS ON JAN. 27, 1994

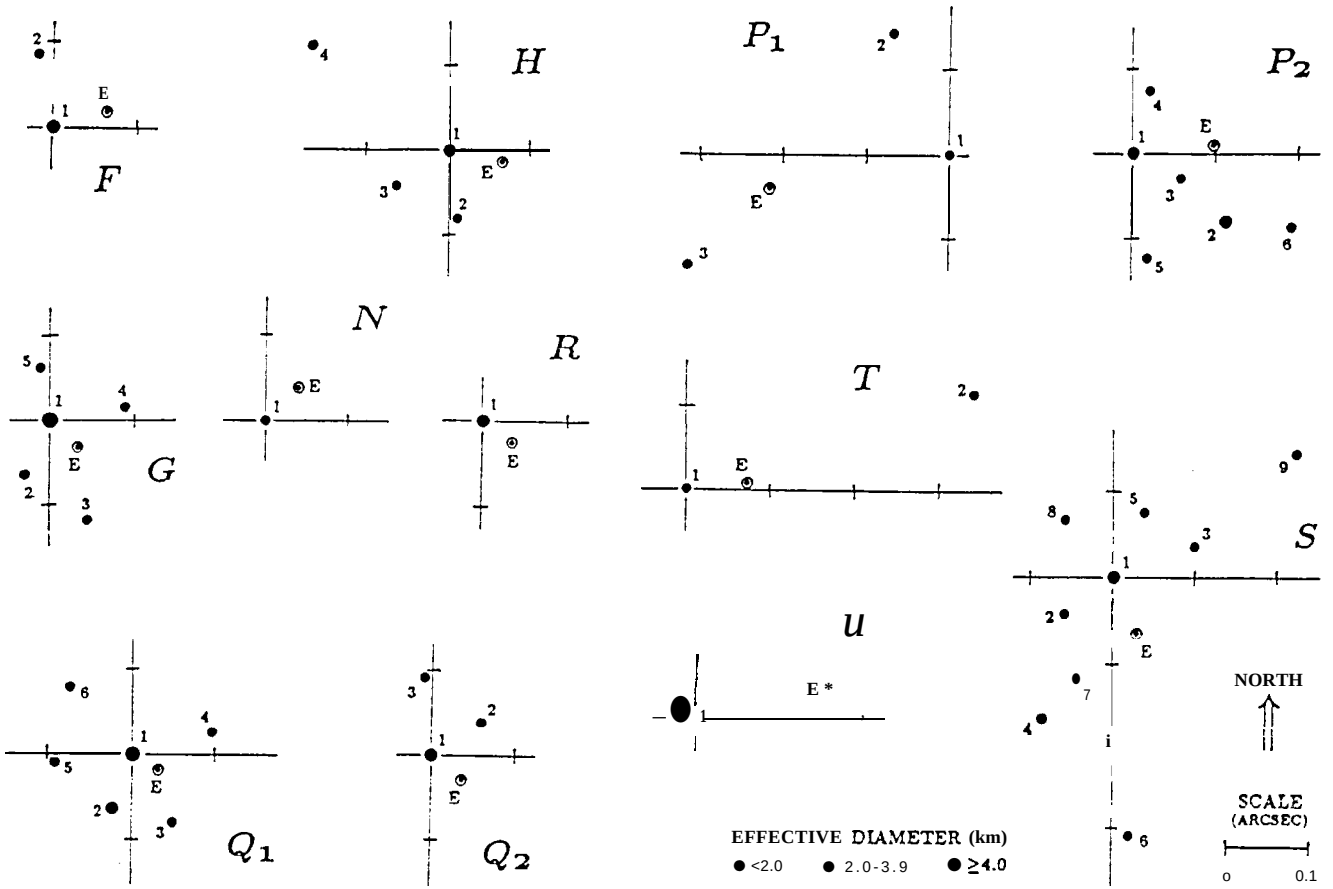

FIG. 2. Projected separations of the companion fragments and the brightness peak of the dust cloud (the extended source) from the brightest fragment in the nuclear condensations F, G, H, N, PI, P_2, Q_1, Q_2, R, S, T, and U, based on the observations made with the HST Planetary Camera on January 27, 1994 and calculated from the analysis of the pixel-brightness distribution near the center of each condensation. The offsets are in the equatorial coordinate system and the angular scale is shown near the bottom-right corner of the figure. At the comet's distance, 0.1 arcsec corresponds to a projected distance of 390 km. The individual fragments are plotted as solid circles of different sizes, correlated with their derived dimensions and are identified by numbers in the order of their decreasing size (Table 4). The locations of the extended-source peaks are plotted as circled dots identifed with the letter E. It is noted that in most condensations the dust cloud is centered on a point that is located in a generally westerly direction from the brightest fragment. Also, several fragments in the condensation S are approximately lined up toward the south.

RELATIVE POSITIONS OF FRAGMENTS AND EXTENDED-SOURCE PEAKS ON MAR. 30, 1994

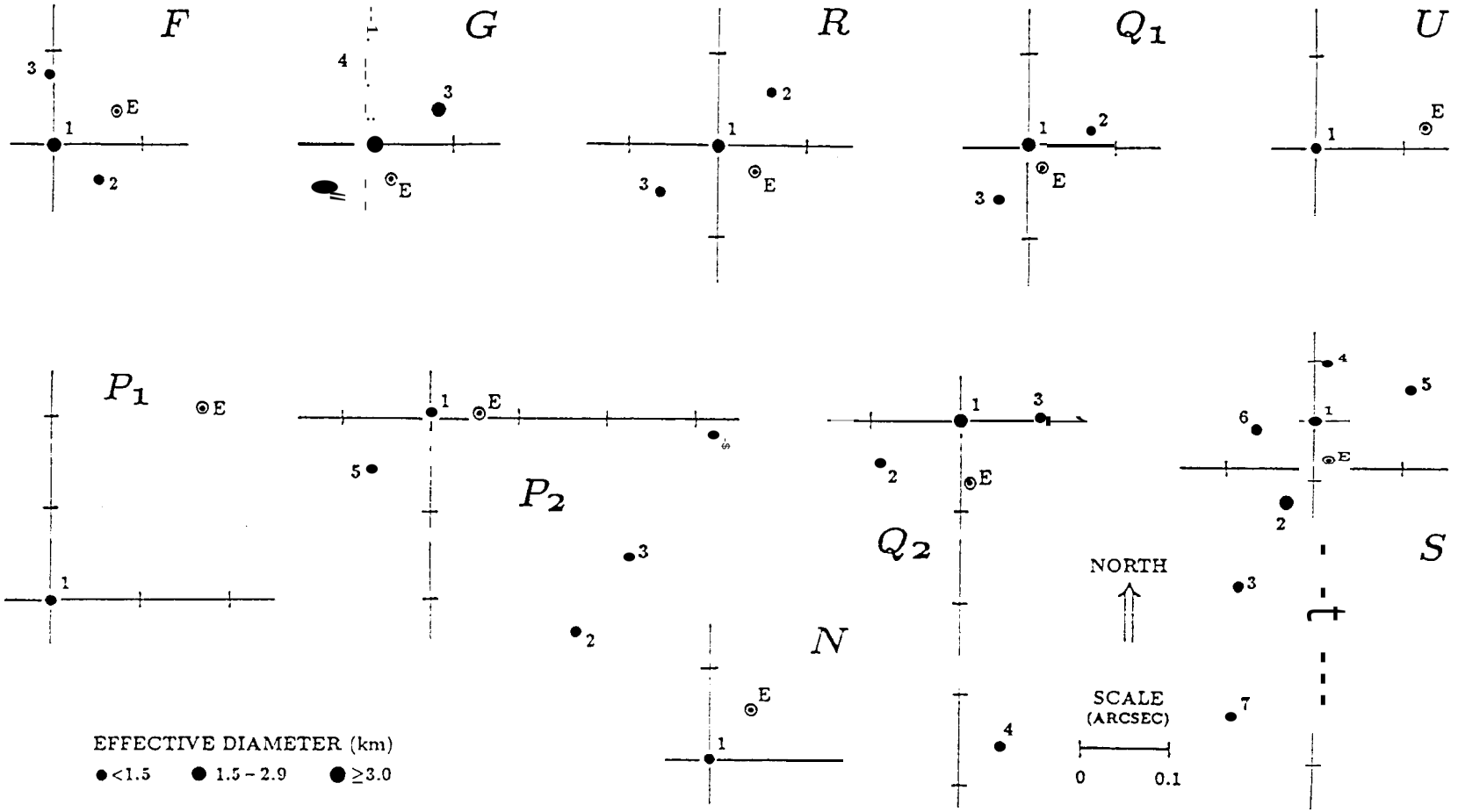

FIG. 3. Projected separations of the companion fragments and the brightness peak of the dust cloud (the extended source) from the brightest fragment in the nuclear condensations F, G, N, P_1, P_2, Q_1, Q_2, R, S, and U, based on the observations made with the HST Planetary Camera on March 30, 1994 and calculated from the analysis of the pixel-brightness distribution near the center of each condensation. For more description, see the caption to Fig. 2. At the comet's distance, 0.1 arcsec corresponds to a projected distance of 327 km. It is noted that, as in Fig. 2, the dust cloud is centered on a point generally to the west of the brightest fragment. Several fragments in the condensation S are still lined up toward the south.

The properties of the PSF approximation are clearly of primary concern in the controversy about the 'photometric'[Y] sizes of the comet's fragments. To obtain a quantitative measure for the sensitivity of the results to the PSF used, I introduced extensive modifications to the law proposed in Sec. 3 and reran several cases with a new law. The idea was to replace the law (1) for the model PSF's surface brightness distribution with a set of quasi-Gaussian functions or, in effect, to postulate that the PSF consists of a sum of "branch" sources. The functions were assumed to have the same parametric values σ_* and ν_* [which replaced, respectively, σ_{psf} and ν_{psf} in (l)] and the distribution of the branch sources was chosen to match the areas of positive pixel-signal residuals in Table 1. The signal of a kth branch source was given by $\Im_k$ and its location defined by {X*+- $\Delta X_k, Y_* + \Delta Y_k$ }, where X_* and Y_* have the same meaning as in (4). The "primary" branch source, of brightness $\Im_0$, contributed most of the PSF's signal and was co-located with the point source itself, that is, $AX_o = AY_o = O$. The other branch sources were introduced to represent appropriate "corrections" to this first approximation. The parameters σ_* and ν_* and the signals $\Im_k(\sigma_*, \nu_*; \Delta X_k, \Delta Y_k)$ were determined by optimizing the fit of this 'composite" quasi-Gaussian law to the model PSF'S pixel-signal distribution. During the solution's iteration it became apparent that the fit could further be significantly improved by adding another branch source, a low-intensity fiat background signal distributed evenly over the entire field of 157 pixels and proportional to the total intensity I_* of the point source. If n_{corr} *is* the number of correction branch sources and $\epsilon << 1$ is the fraction of I_* contained in the flat distribution, the approximation to the total signal in the PSF by a composite quasi-Gaussian distribution law can formally be optimized by requiring that

$$I^* = d^* + \sum_{k=0}^{n_{corr}} \Im_k(\sigma_*, \nu_*; \Delta X_k, \Delta Y_k). \tag{lo}$$

Since the signals of the correction branch sources, $\Im_k (k = 1,2,.\ ,., n_{corr})$ can be written in terms of the primary branch source's signal $\Im_0$,

$$\Im_k = \epsilon_k \Im_0 \ (\epsilon_k \ll 1; k = 1, 2, \ . \ . \ ., n_{corr}), \tag{11}$$

and since one always can find a constant $\epsilon_{flat} << 1$ that satisfies a condition $\epsilon_{flat}\Im_0 = \epsilon I_*$, the expression (1 O) can be rewritten in the form:

$$I_* = \Im_0 \left(1 + \epsilon_{flat} + \sum_{k=1}^{n_{corr}} \epsilon_k\right) \tag{12}$$

The selected and optimized composite quasi-Gaussian law approximation to the P S F consisted of 10 branch sources: a primary one, a flat one, and 8 correction ones. Most parameters are listed in Table 8, except for the signal of the primary component, which was found to amount to $\Im_0 = 0.6341*$, and the optimized values of the common parameters, which came out to be $\sigma_* = 0.0184$ arcsec and $\nu_* = 0.528$, so the surface-brightness distribution functions of the branch sources were close to an exponential. Compared with the law proposed in Sec. 3, the fit to the model PSF was improved significantly, leaving for a point source of $I_* = 500$ ADU a mean pixel-sig])al residual of ± 0.58 ADU (compared with ± 0.86 ADU for the approximation in Sec. 3) and, as seen from the new distribution of the PSF residuals over the 157 pixels in Table 9, a maximum residual of 2 ADU (compared with 3 ADU before).

TABLE 8

Parameters of the Flat and Correction Branch Sources of the PSF's Beat-Fit Composite Quasi-Gaussian Law Approximation.

Branch source, k	ϵ_k	ΔX_k (pixels)	ΔY_k (pixels)	Branch source, k	ϵ_k	ΔX_k (pixels)	ΔY_k (pixels)	Branch source, k	ϵ_k	ΔX_k (pixels)	ΔY_k (pixels)
flat	0.0991	...	...	3	0.0667	−1.75	+1.75	6	0.0539	−1.75	−0.25
1	0.0886	0.00	+1.75	4	0.0605	+1.75	+1.75	7	0.0454	+2.00	−1.50
2	0.0684	+2.00	0.00	5	0.0593	−0.25	−1.75	8	0.0357	−1.75	−1.75

The application of the new PSF approximation law to the January 1994 digital maps for the condensations G and H yielded results that differed insignificantly from those based on the law of Sec. 3. The signals of the major fragments were reproduced to within 1 percent or so and their locations to within 0.01 pixel! For the companion fragments the uncertainties were found to increase with decreasing signal, for the faintest detected ones the differences reaching up to a few tens percent of the signal and up to several tenths of a pixel in the position. It appears that only on rare occasions do the two approximations lead to major disagreements in that a very faint companion is "picked up" by the iterative approach when using one of the two laws but is missed when employing the other.

TABLE 9

Pixel Distribution of the Brightness Residuals (in ADU) From the PSF'S Best-Fit Composite Quasi-Gaussian Law Approximation for a Point Source Whose $I_* = 500$ ADU.

X (pixels)	Y (pixels) 3	4	5	6	7	8	9	10	11	12	13	14	15	16	17	X (pixels)
3							0	0	0							3
4					0	0	0	0	0	0	()					4
5				0	0	0	0	0	0	0	0	0				5
6			"	0	0	0	0	0	0	0	0	0	o			6
7		0	0	0	0	o–1	o	o–1	o	0	0	0				7
8		0	0	0	0-1	0	−1	+2	−2	−1	0	0	0			8
9	0	0	0	0	0	+1	−2	+1	−2	+2	0	0	0	0	0	9
10	0	0	0	0	0	−1	+1	+1	o–1	()	o	0	0	0		10
11	0	0	0	0	0	+	1	-	2	o	−2	+2	o	0	0	0	0	11
12		0	0	0	0	−1	+1	−1	+2	−2	0	0	0	0		12
13		0	0	0	0	−	1	−	1	−	1	0	−	1	0	0	0	13
14			0	0	0	0	0	0	0	0	0	0	0			14
15				0	0	0	0	0	0	0	0	0				15
16					0	0	0	0	0	0	()					16
17							0	0	0							17

The maps of the pixel-signal residuals remained virtually unchanged in comparison with those yielded by the PSF's approximation applied in Sec. 3 (cf. Tables 6 and 7 for the condensation H). Specifically, the introduction of the first point source again eliminated the prominent clump of positive residuals centered on the pixel { 10, 9} and the subsequent introduction of additional sources removed the systematic trend from negative to positive residuals across the entire field. Initially (when solving for an extended source only), these effects were so pronounced and so distinctly nonrandom that they could not possibly be products of instrumental noise,

The evidence presented in this study leads to the following conclusions: (1) the steep slope of the observed surface-brightness distribution in the immediate proximity of the peak pixel is due primarily to the presence of an unresolved sou rce--a major fragment—and not an effect of the spatial density of particulate that increases rapidly toward the center of the dust cloud; (2) the derived signals of the major fragments are rather insensitive to the approximations employed for the PSF and for the brightness distribution in the extended source; and (3) the largest fragments detected on three different dates between late January and early July 1994 are about 4 km across for an assumed geometric albedo of 4 percent and a phase coefficient of O.O35 mag/deg. These conclusions corroborate the earlier findings by Weaver *et al.* (1994) and confirm my preliminary results on the continuing presence of massive objects in the condensations, as published shortly before the impacts with Jupiter (Sekanina 1994), but they appear to be contrary to Weaver's (1994a) more recent conclusions and are grossly incompatible with all estimates of less than about 7–8 km for the effective diameter of the progenitor comet.

The findings on the companion fragments listed in Table 4 are less conclusive. Relative to the major fragments, the intrinsic brightness of these objects is generally less well determined and the existence of some of them may even be in doubt. Because of these uncertainties and because of potentially hidden instrumental effects that might affect the conclusions of the present investigation, it is prudent to view the results presented here as still somewhat preliminary. However, I submit that evidence underlying the fundamental conclusions of this study is robust and that any circumstances severely affecting them would have to be substantial. In any case, one cannot err by expressing belief that attention will remain focused on the problem of analysis of the HST digital maps as one of the most hopeful avenues in our quest for solving the problem of the dimensions of—and the energy deposited in the jovian atmosphere by—Comet Shoemaker- Levy 9.

8. ACKNOWLEDGEMENTS

I thank H. A. Weaver for his kindly providing digital maps for the 13 nuclear condensations of Comet Shoemaker- Levy 9, which were secured with the WFPC-2; for extensive information on the processing, calibration, and noise characteristics of the HST images; and for his expert comments on the results of the present investigation. This work is based on observations made with the NASA/ESA Hubble Space Telescope obtained at the Space Telescope Science Institute (STScI), which is operated by the Association of Universities for Research in Astronomy, Inc., under contract with the National Aeronautics and Space Administration. This research was carried out by the Jet Propulsion Laboratory, California Institute of Technology, under contract with the National Aeronautics and Space Administration and was supported in part through Grants GO- 5021 and GO-5624 from the STScI.

REFERENCES

Asphaug, E. & Benz, W. (1.994). Density of comet Shoemaker-Levy 9 deduced by modelling breakup of the parent "rubble pile". *Nature* 37o, 120--124.

Chernetenko, Y. A. & Medvedev, Y. D. (1994). Estimate of the Shoemaker–Levy 9 nucleus size from position observations. *Planet.* Space *Sci.* 42, 95–96.

Scotti, J. V. & Melosh, H. J. (1993). Estimate of the size of comet Shoemaker–Levy 9 from a tidal breakup model. *Nature 365, 733-735.*

Sekanina, Z. (1994). Periodic comet Shoemaker–Levy 9 (1993e). *IA U Circ. No. 6020.*

Sekanina, Z., Chodas, P. W. & Yeomans, D. K. (1994). Tidal disruption and the appearance of periodic comet Shoemaker-Levy 9. *Astron. Astrophys.* 289, 607–636.

Solem, J. C. (1994). Density and size of comet Shoemaker–Levy 9 deduced from a tidal breakup model. *Nature* 37o, 349–351.

Weaver, H. A. (1994a). Periodic comet Shoemaker--Levy 9 (1993e). *IA U Circ. No.* 5947.

Weaver, H. A. (1994b). Periodic comet Shoemaker--Levy 9 (1993e). *IA* U *Circ. No.* 5973.

Weaver, H. A., Feldman, P. I)., A'Hearn, M. F., Arpigny, C., Brown, R. A., Helin, E., F., Levy, D. H., Marsden, B. G., Meech, K. J., Larson, S. M., Nell, K. S., Scotti, J. V., Sekanina, Z., Shoemaker, C. S., Shoemaker, E. M., Smith, T. E., Storrs, A. D., Yeomans, D. K. & Zellner, B. (1994). Hubble Space Telescope observations of comet P/Shoemaker-Levy 9 (1993 e). *Science 263, 787-791.*